Supplement of Hydrol. Earth Syst. Sci., 29, 1725–1748, 2025
https://doi.org/10.5194/hess-29-1725-2025-supplement

Hydrology and Earth System Sciences
Open Access
EGU

Supplement of

Scale dependency in modeling nivo-glacial hydrological systems: the case of the Arolla basin, Switzerland

Anne-Laure Argentin et al.

Correspondence to: Anne-Laure Argentin (aargentin@unibz.it)

S1. Model structure of Hydrobricks and study area discretization

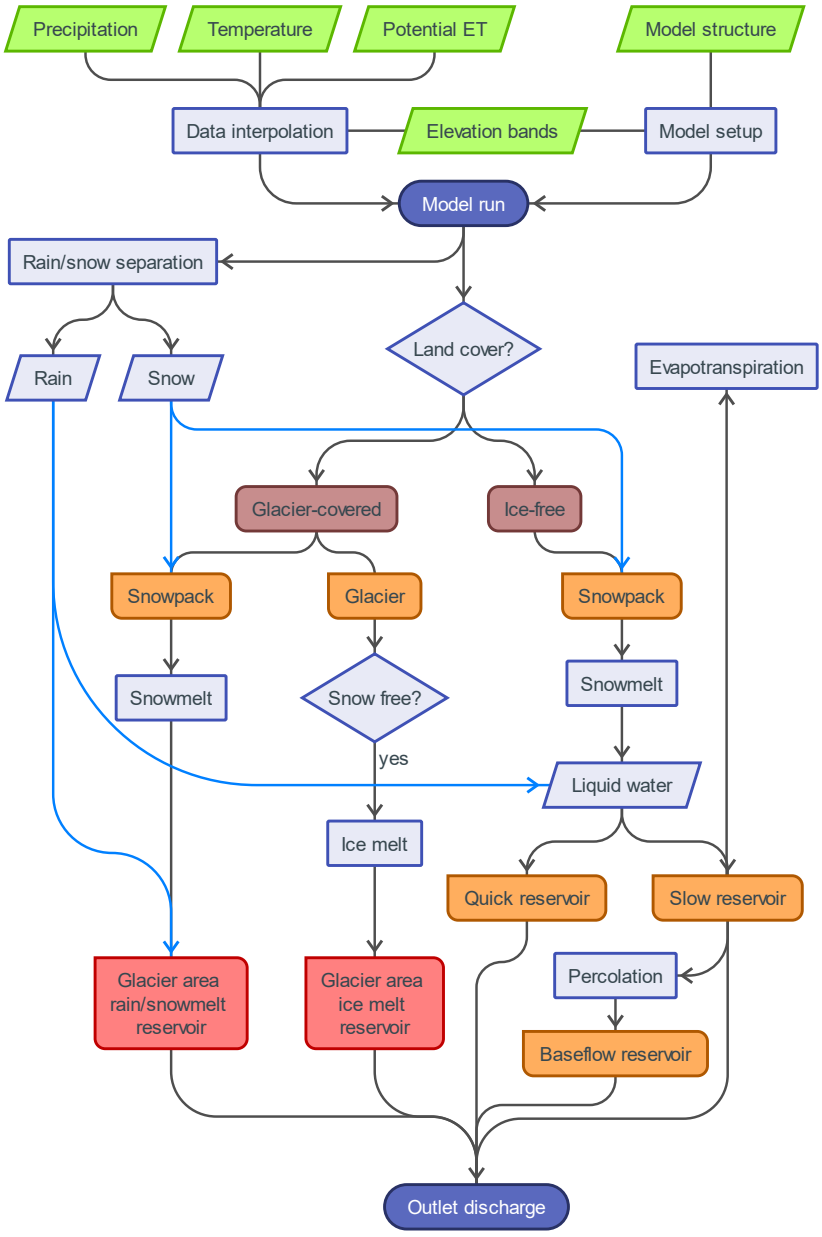

Figure S1. Illustration of the Hydrobricks model workflow used in this study. The glacier-covered part illustrates the behavior of both the bare ice and debris-covered glaciers. Orange reservoirs are distributed over all elevation bands and red reservoirs are lumped over the catchment. Figure taken from Shokory et al. (2023).

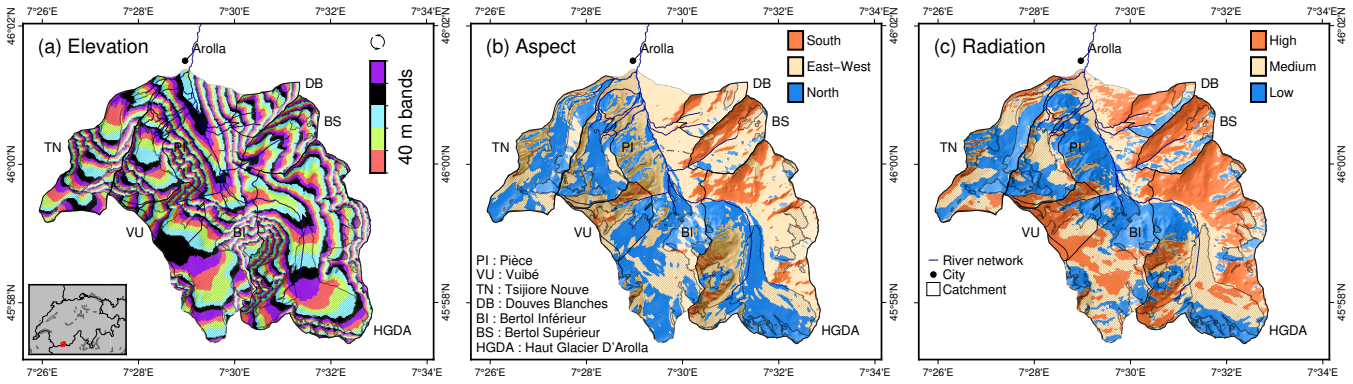

Figure S2. Hydrobricks' hydrological units for the whole catchment, discretized (a) according to elevation to use in the classic temperature-index (TI) model, (b) according to aspect to use in combination with elevation discretization in the aspect temperature-index (ATI) model (c) according to mean annual potential clear-sky direct solar radiation with cast shadows to use in combination with elevation in the Hock temperature-index (HTI) model.

S2. Geology of the study area and characteristics of the catchments

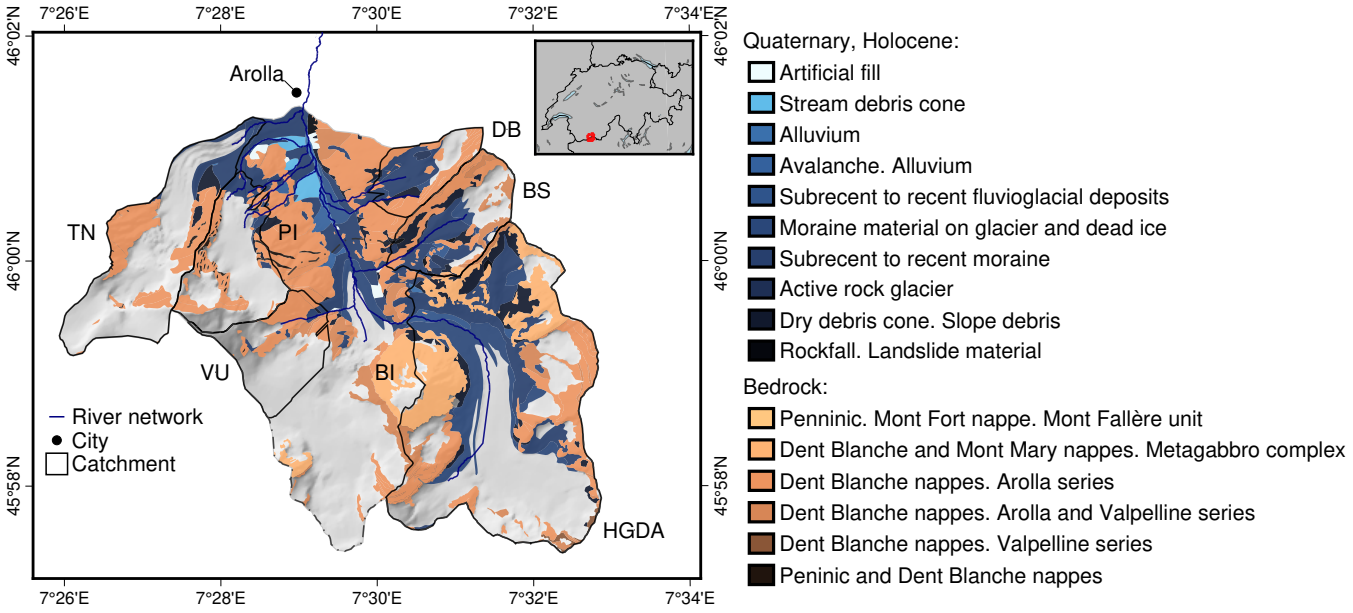

Figure S3. Geological cover of the study area, and of the different subcatchments, extracted from the GeoCover V2 product (SwissTopo, 2024).

Catchment	Minimum elevation (m)	Maximum elevation (m)	Mean elevation (m)	Standard deviation elevation (m)	Mean catch. slope
Whole	2183	3789	3085	289	29.3
BI	2183	3722	3063	229	28.7
HGDA	2582	3677	3014	191	29.5
TN	2289	3789	3180	443	28.2
PI	2636	3784	3046	266	27.8
BS	2913	3583	3127	117	32.4
VU	2730	3722	3036	152	24.7
DB	3097	3364	3218	58	35.4

Table S1. Basic statistics on the topography of the glaciated areas (2016) of each catchment.

Catchment	Mean (glaciated)	SD (glaciated)	Mean (catchment)	SD (catchment)
Whole	356.3	60.6	341.1	93.7
BI	347.9	59.1	323.4	95.4
HGDA	343.1	56.0	304.3	97.7
TN	12.6	57.1	15.4	64.5
PI	24.7	53.5	28.7	61.5
BS	238.9	43.5	237.7	72.4
VU	38.4	63.0	64.9	72.2
DB	249.7	23.4	259.2	48.9

Table S2. Circular means and standard deviations of the aspect over the glaciated areas (2016) and total areas of each catchment, computed with the zonal statistics of ArcGIS. SD: Standard deviation.

Catchment	Debris cover area (km^2)	Glacier area (km^2)	Debris coverage percentage
BI	1.00	10.04	9.9%
HGDA	0.69	4.22	16.3%
TN	0.56	2.76	20.4%
PI	0.29	1.66	17.3%
BS	0.03	0.24	14.3%
VU	0.02	1.21	1.4%
DB	0.04	0.15	23.9%

Table S3. Debris cover areas, glaciated areas and debris cover percentage for each catchment for the year 2016.

S3. Additional results with the ATI melt model

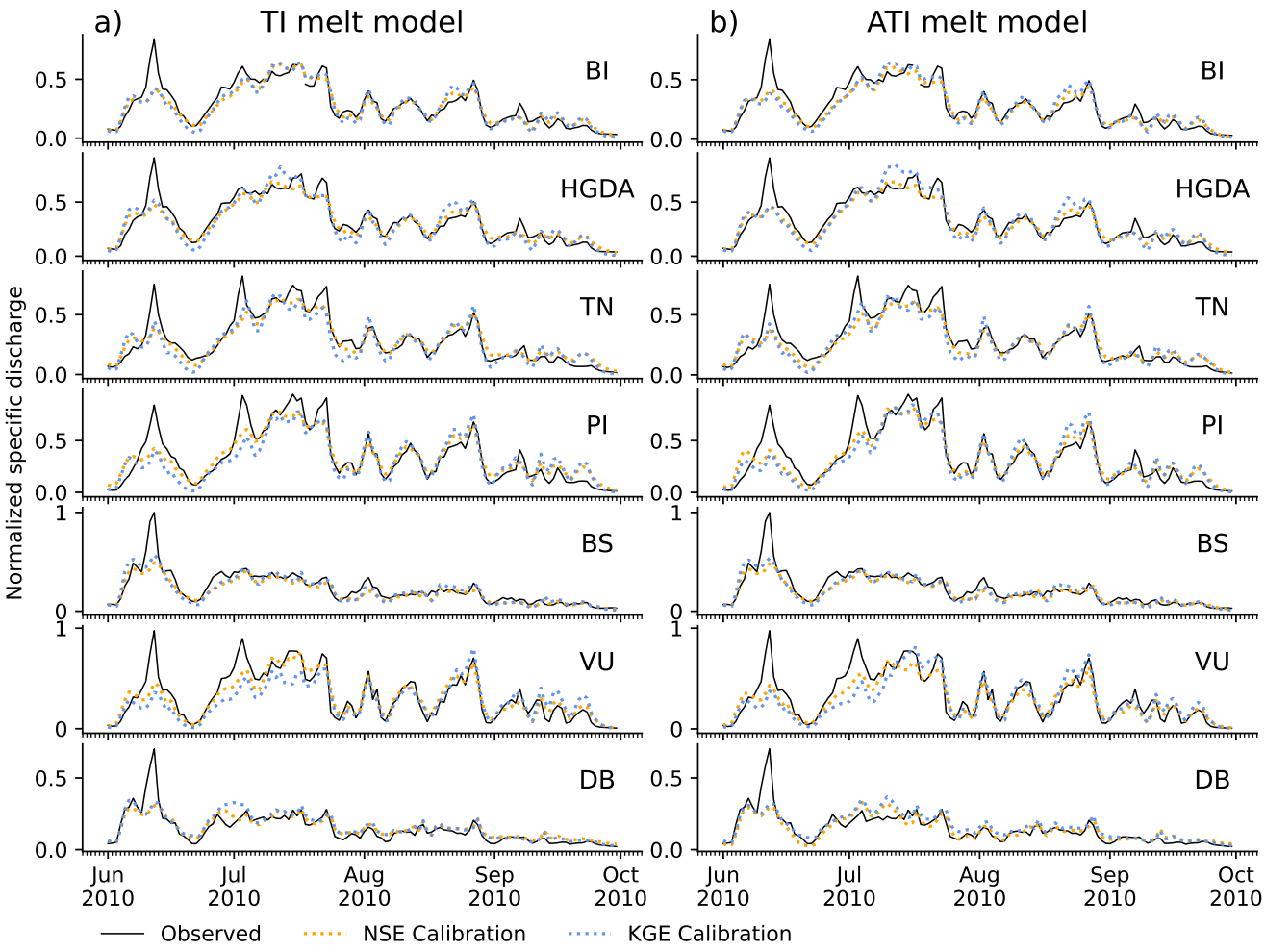

Figure S4. Observed and simulated hydrographs for all catchments for 2010 with the a) TI and b) ATI melt models. Observed discharge (black solid line) is compared to the calibration run using NSE (dotted orange) and KGE (dotted blue). Specific discharge (unit: mm) is normalized to the highest value.

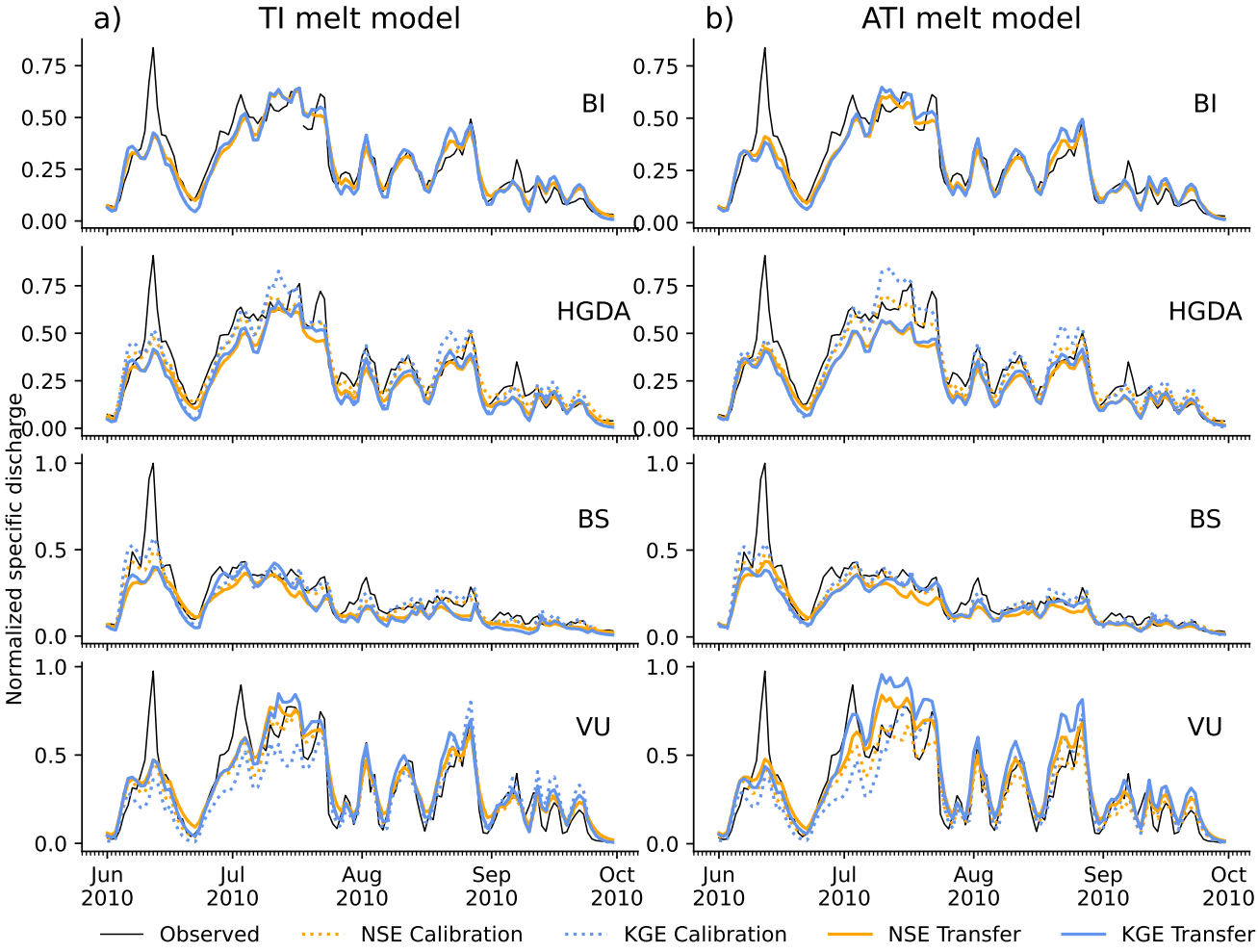

Figure S5. Observed and simulated hydrographs of the BI catchment and its nested subcatchments for 2010 with a) TI and b) ATI melt models. Observed discharge (solid black line) is compared to the calibration runs and to the transfer runs with the calibrated parameters of BI: Shown are the results for NSE (orange) and KGE (blue); dotted lines show the calibration runs, solid lines show the transfer runs. For BI, the calibration and transfer runs are identical. Specific discharge (unit: mm) is normalized to the highest value.

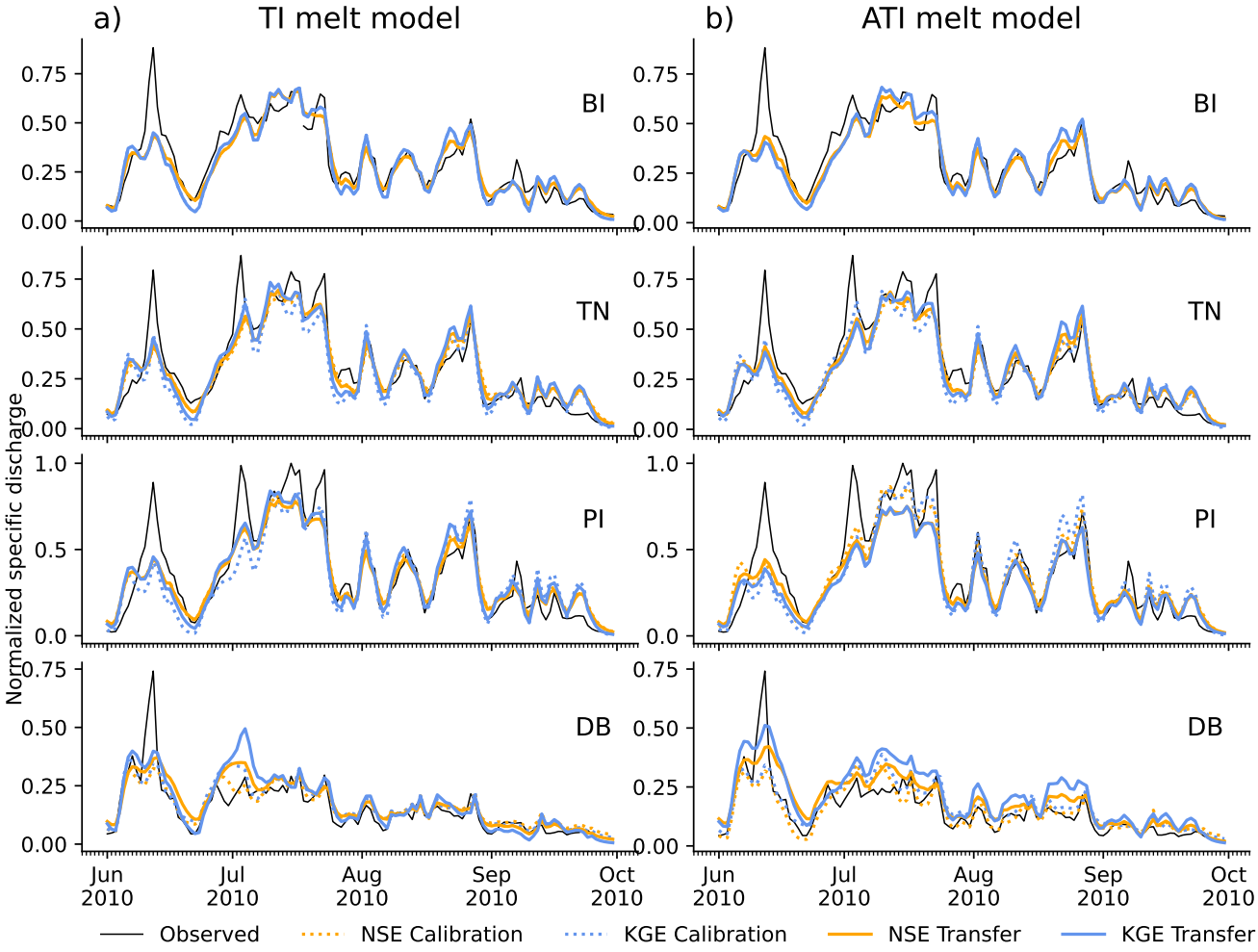

Figure S6. Observed and simulated hydrographs of the BI catchment and its neighboring catchments for 2010 with a) TI and b) ATI melt models. Observed discharge (solid black line) is compared to the calibration run and to the transfer runs with the calibrated parameters of BI: Shown are the results for NSE (orange) and KGE (blue); dotted lines show the calibration runs, solid lines show the transfer runs. For BI, the calibration and transfer runs are identical. Specific discharge (unit: mm) is normalized to the highest value.

S4. Debris cover mapping

The GLAMOS dataset offers both debris-free ice extent and glacier extent for 2016, but only glacier extent for 2010 and previous years (Linsbauer et al., 2021; Fischer et al., 2014). To obtain the debris-free ice extent trend since 2010, we relied on the debris-free ice detection algorithm from (Shokory and Lane, 2023), now available under ArcGIS Pro. We applied it to compute the corresponding debris-free ice extents for the 2010 GLAMOS dataset, thus allowing us to infer the debris cover evolution from 2010 to 2016. No estimates of debris cover thicknesses were available.

Given the suboptimal conditions of Landsat 7 images in 2010 for mapping, we opted for an image from 2009. Two images, dated 06/09/2009 and 22/09/2009, displayed minimal cloud cover and limited snow patches. Between the two, the 06/09/2009 image displayed the smallest swath gaps. We corrected the Landsat 7 Level 1 near infrared (NIR)-B4 and shortwave Infrared (SWIR)-B5 bands, both available at 30m resolution, for top of atmosphere reflectance with solar angle correction. To do so, we applied the radiometric rescaling coefficients given in the associated metadata files provided with the Landsat Level-1 NIR and SWIR bands. We then applied the methodology of Shokory and Lane (2023) that uses the condition $\frac{NIR}{SWIR} \geq t$, with NIR representing the Near Infrared band, SWIR the Shortwave Infrared band, and t denoting the threshold condition for debris-free ice delineation. We tested incremental thresholds with steps of 0.05 between 1.00 and 3.00 and determined that a threshold value t of 2.00 provided the best results in the transition areas between debris-free ice and debris-covered ice (in brown, Fig. S7). We nonetheless had to manually correct for the influence of the swath gaps (in red, Fig. S7).

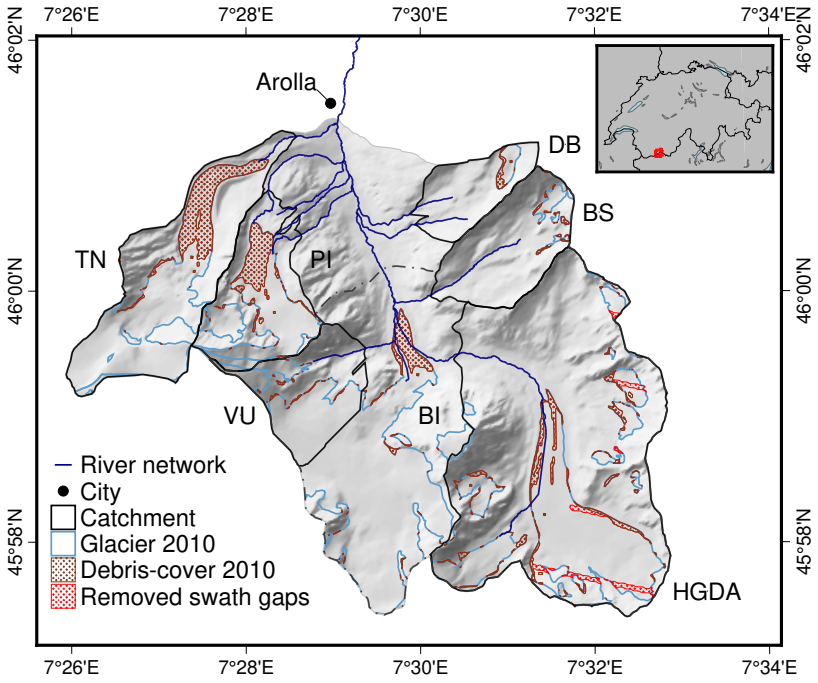

Figure S7. The mapped 2010 debris cover extent is indicated in brown, and the GLAMOS 2010 glacier extent in blue (Fischer et al., 2014). The manually removed debris linked to the swath gaps are indicated in red.

S5. Additional results with debris cover

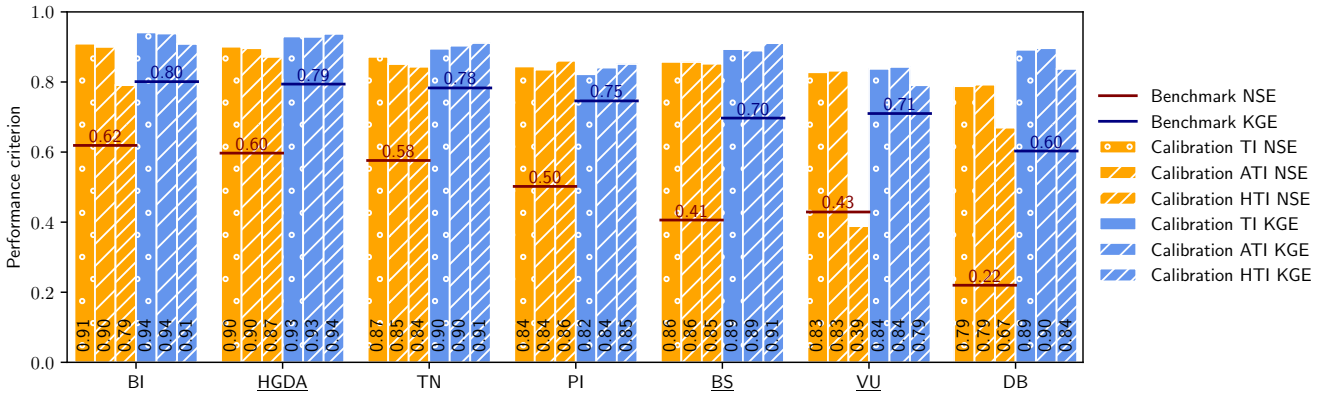

Figure S8. Comparison of the performance of the three melt models on the seven catchments, quantified either by the Nash–Sutcliffe efficiency (NSE, orange bars) or by the Kling-Gupta efficiency (KGE, blue bars) performance criteria of observed and simulated discharges for the period 2010-2014. For comparison, the benchmark NSE and KGE are computed and plotted as red and dark blue thresholds, respectively. The simulations are run 10000 times over the years 2009 - 2014, with 2009 the calibration year. Catchments are ordered by area, from BI (largest) to DB (smallest). All performance criteria are computed on the 2010-2014 time period.

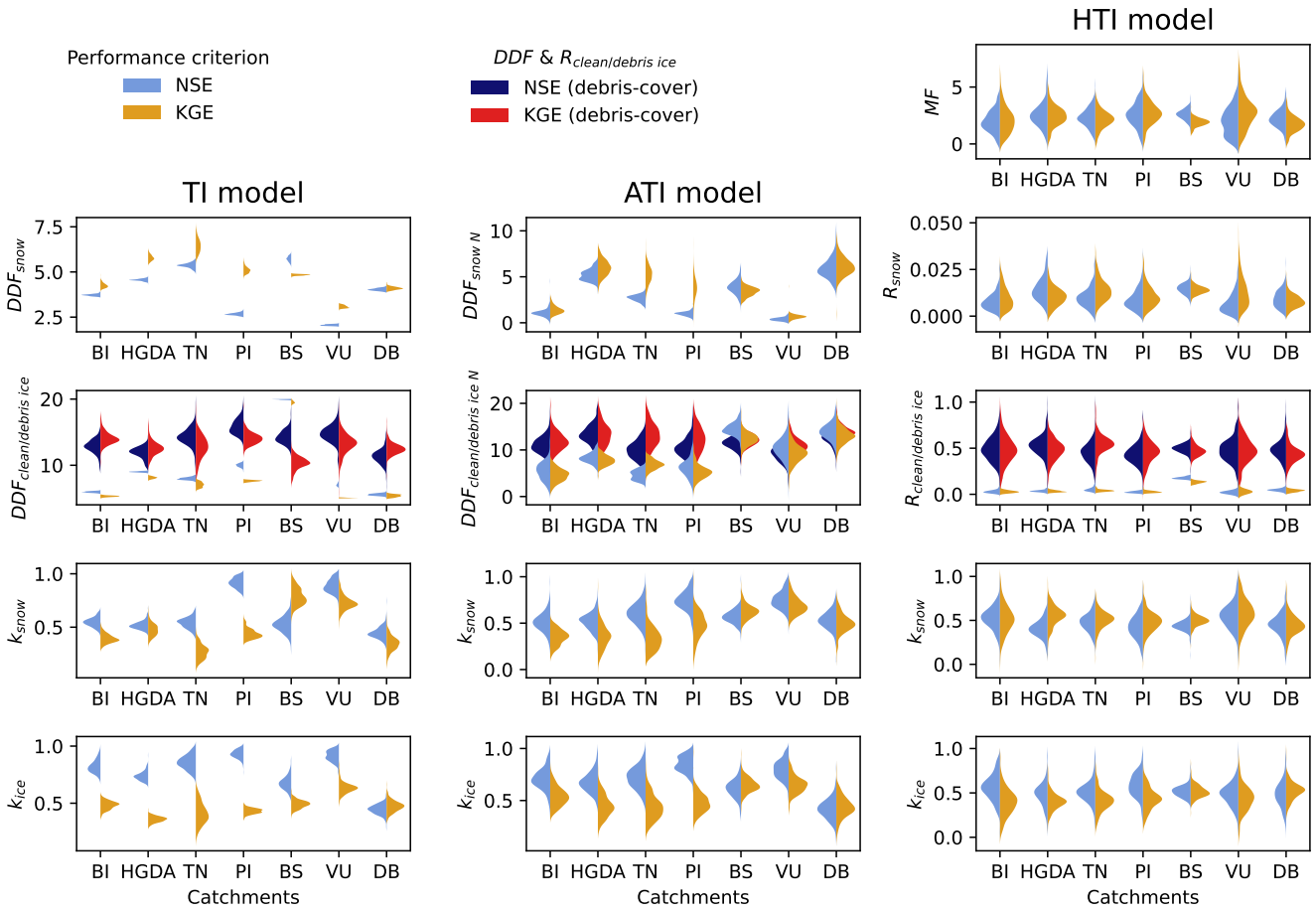

Figure S9. Obtained ice and snow parameters for the best 5% NSE and KGE scores for all catchments, with the three melt models and the two performance criteria.

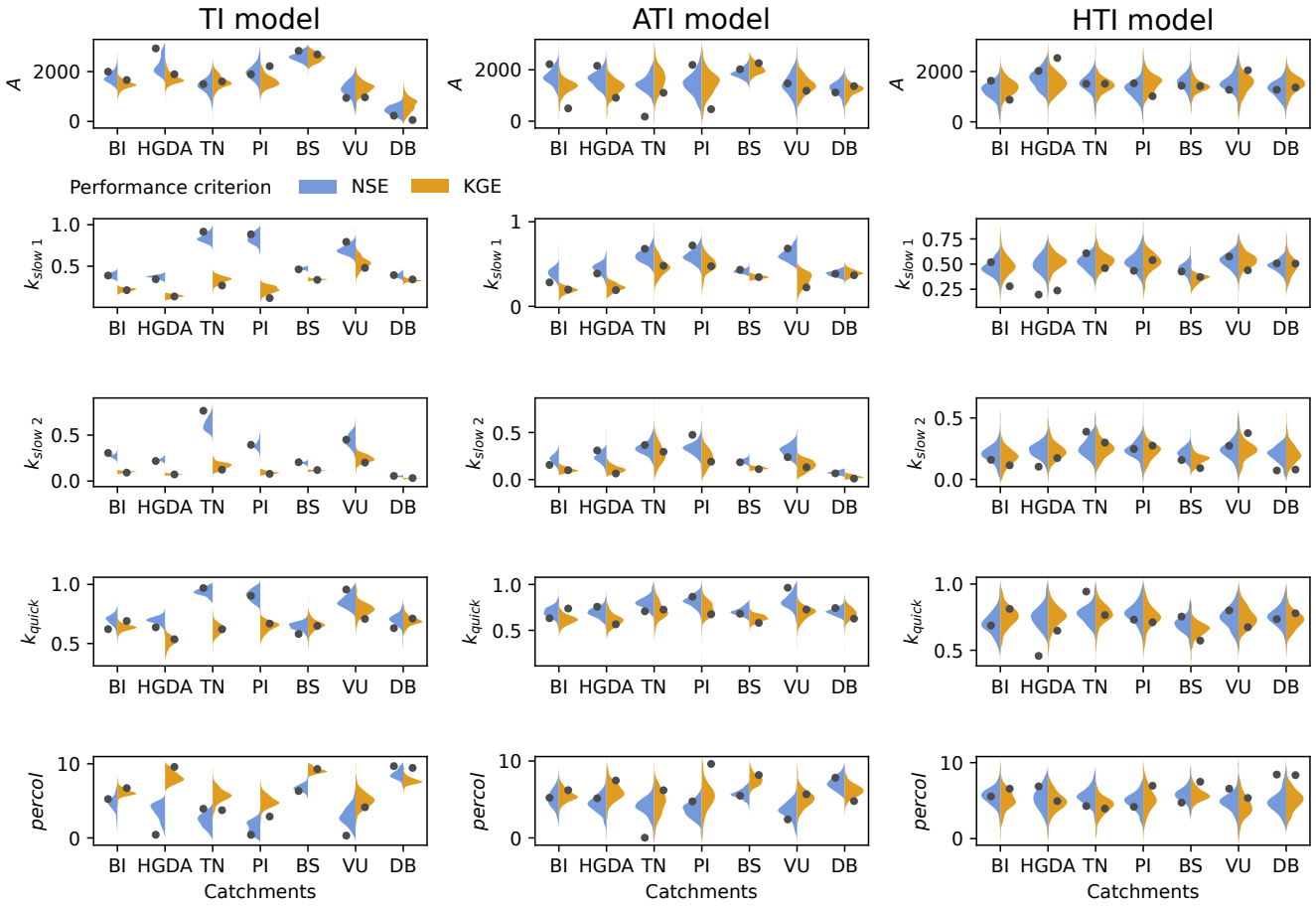

Figure S10. Obtained ground parameters for the best 5% NSE and KGE scores for all catchments, with the three melt models and the two performance criteria. The parameter set values achieving the best NSE and KGE scores are plotted on top with a dot. Catchments are ordered by area, from BI (largest) to DB (smallest).

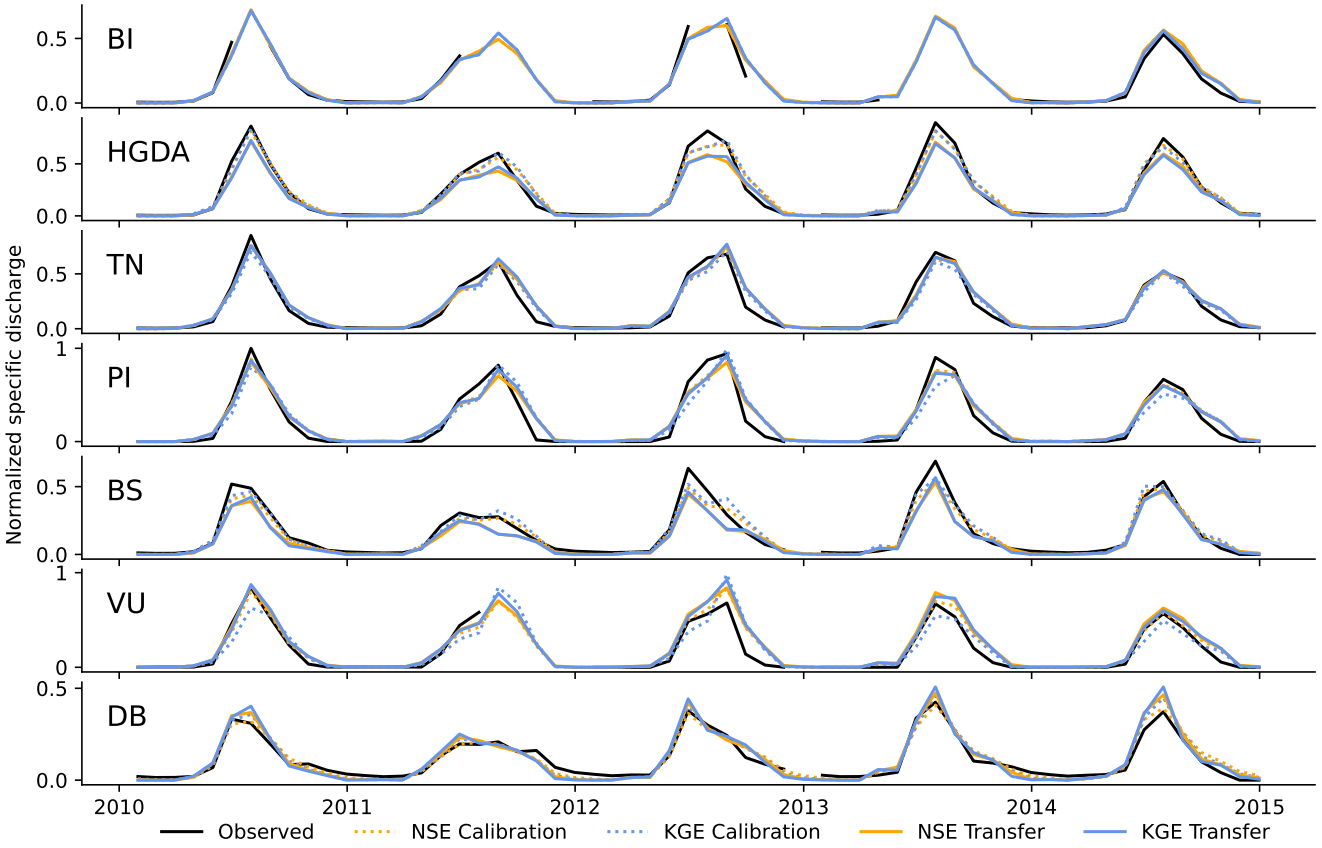

Figure S11. Monthly water hydrographs for the TI melt model on the seven catchments, calibrated or transferred through the application of the parameter set of BI. The original observed dataset (black) is compared to the calibration run using the NSE (dotted orange) and the KGE (dotted blue), and with the transfer run with the calibrated parameters found in the BI catchment with the NSE (orange) and the KGE (blue). Observed monthly yields with missing discharge values are not computed. Specific discharge (unit: mm) is normalized to the highest value.

S6. Precipitation patterns

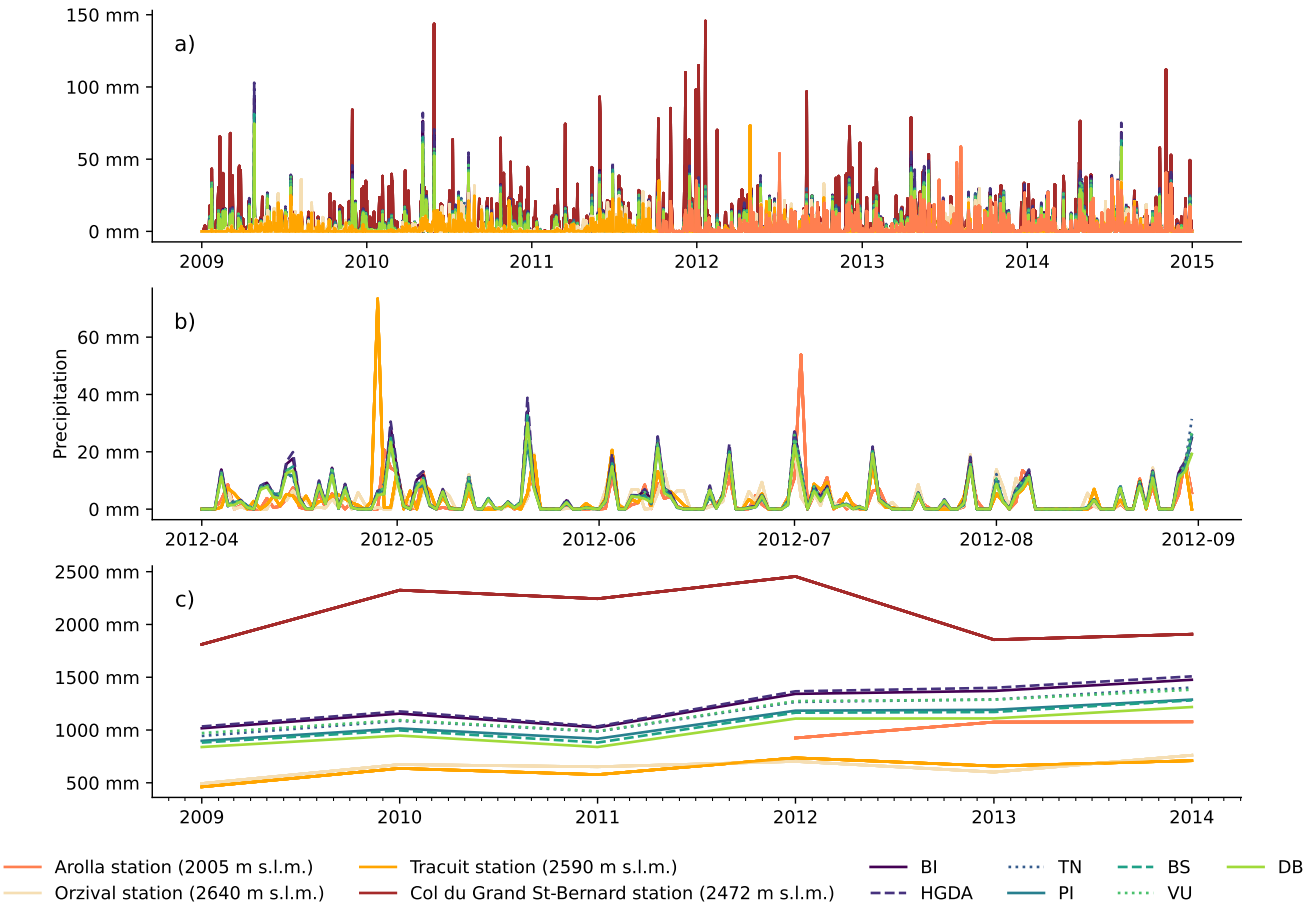

Figure S12. Comparison of the precipitation patterns at the Arolla station with the daily mean precipitation patterns for each catchment. Comparison at the daily scale (a) over the model time period, with the Arolla station data only becoming available end of 2011, (b) over the year 2012, and (c) at the annual scale, over the model time period. Orzival station: 20 km NNE of Arolla station. Tracuit station: 18 km NE of Arolla station. Col du Grand St-Bernard station: 29 km SW of Arolla station.

S7. Discharge patterns

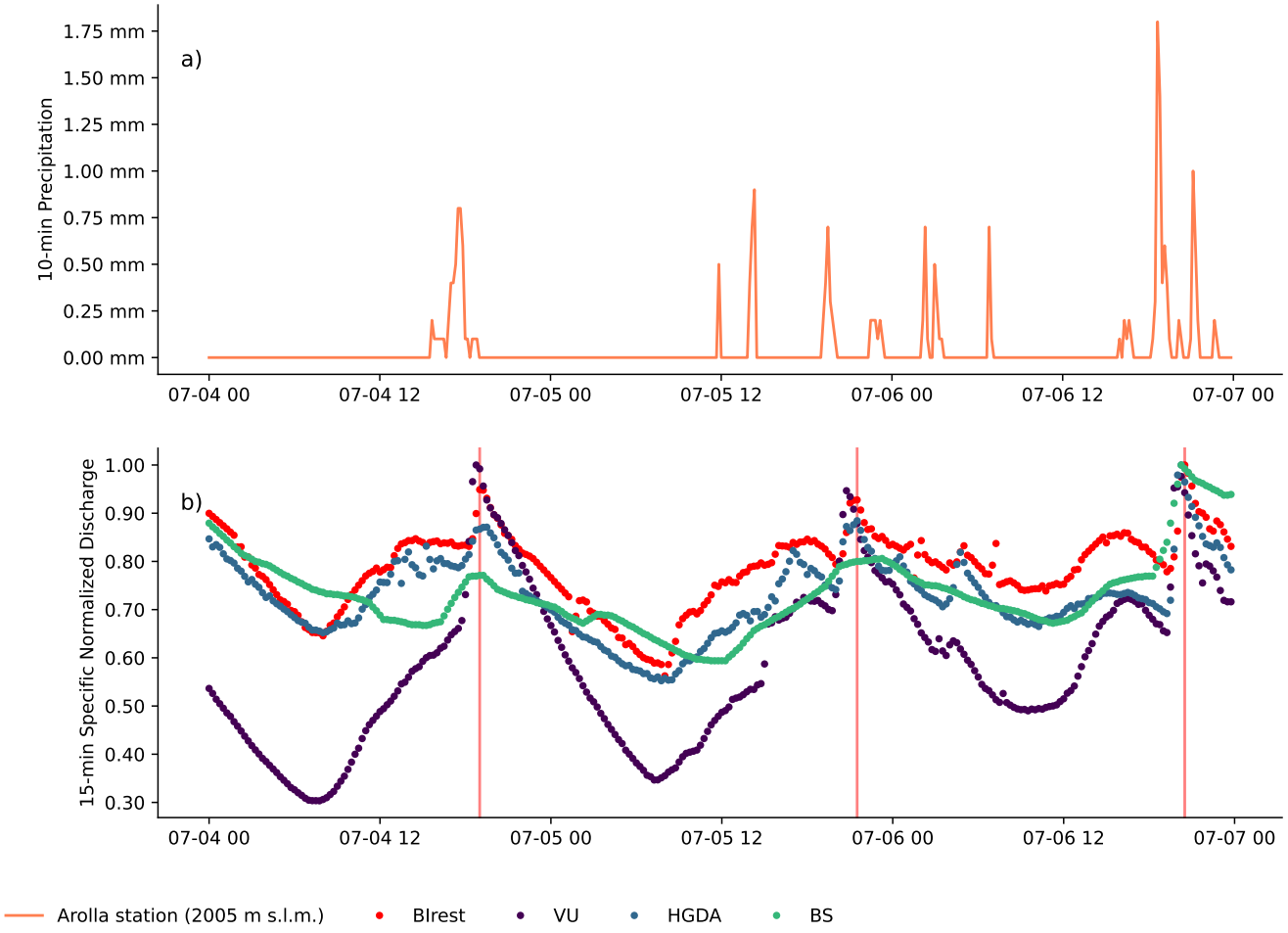

Figure S13. Comparison of (a) the 10-minute precipitation patterns at the Arolla station with (b) the 15-minute normalized specific discharge patterns for the BI intake (called BIrest) and its upstream intakes: VU, HGDA and BS. The vertical lines indicate the time of maximum discharge for the BI intake for each day, and highlight that the water takes around 15-30 minutes to reach the BI intake from the upstream intakes.

S8. Patterns of water fluxes and retention

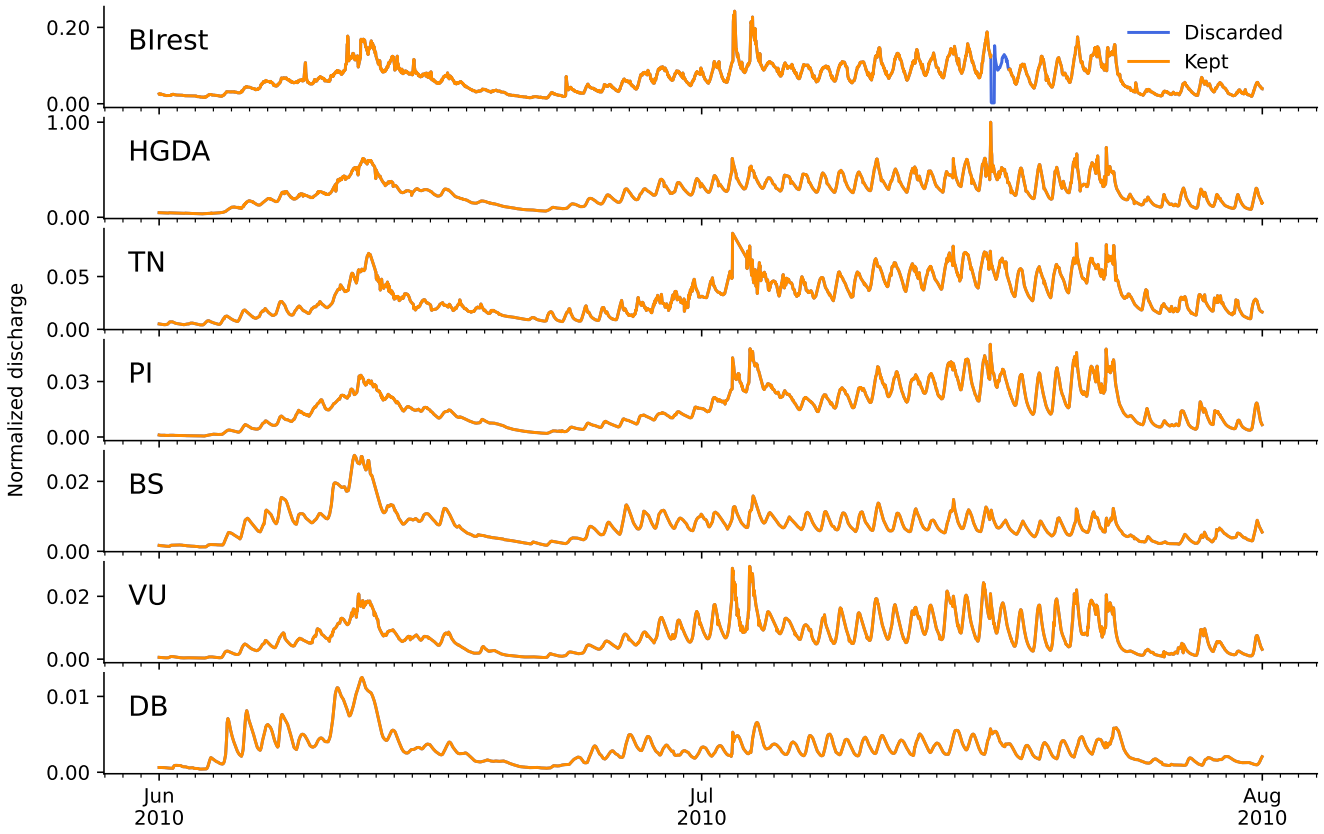

Figure S14. Comparison of the discharge series kept for calibration in Hydrobricks (orange) with the discarded periods (blue), over the summer 2010. Analysis according to Swift et al. (2005) leads to the interpretation that glacial snowpack was removed from mid-June on, allowing diurnal discharge patterns to take on a peaked shape. Discharge (unit: $m^3\ s^{-1}$) is normalized to the highest value.

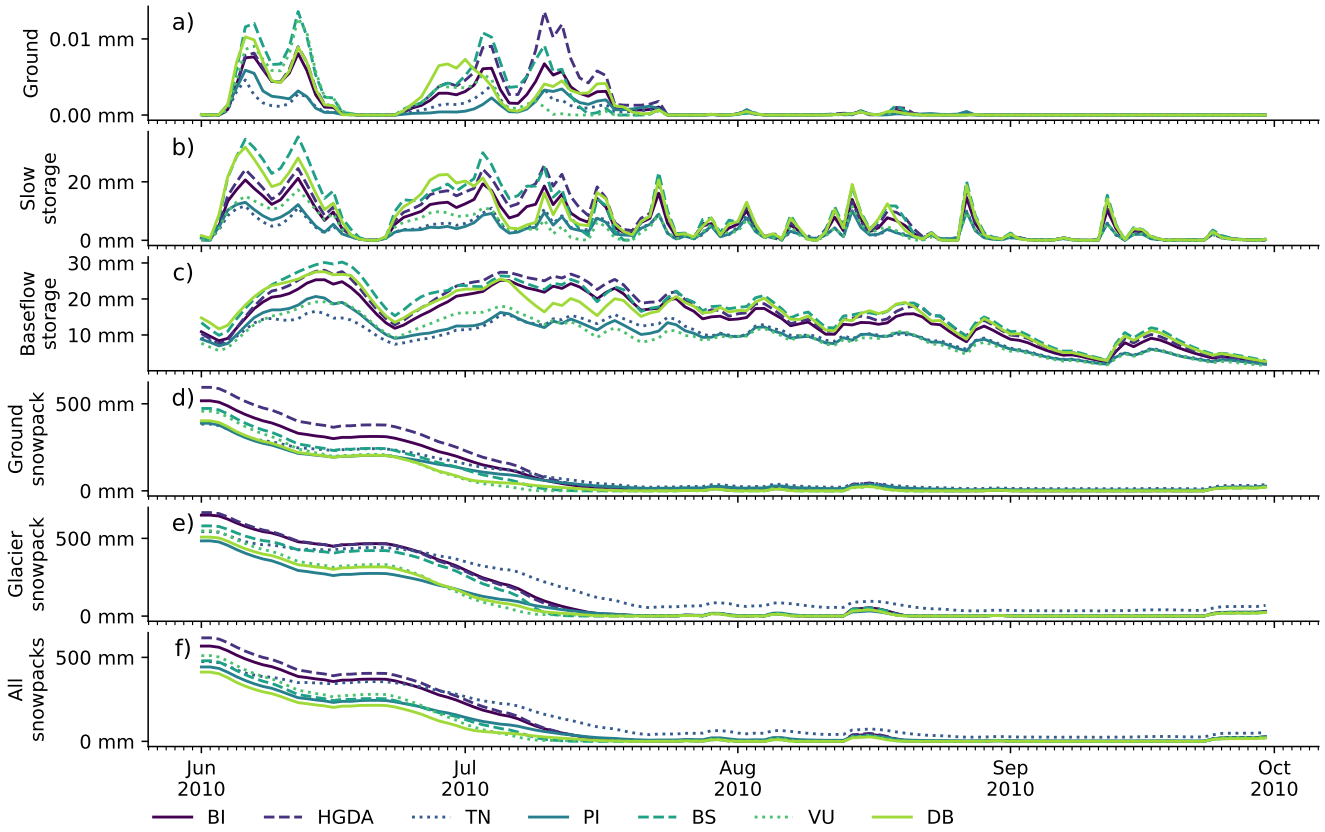

Figure S15. Modeled water content heights in the a) ground, b) slow storage and c) baseflow reservoir, and modeled snow water equivalent on the d) ground, e) glacier and f) ground and glacier during the summer 2010. Water heights are computed on their respective areas.

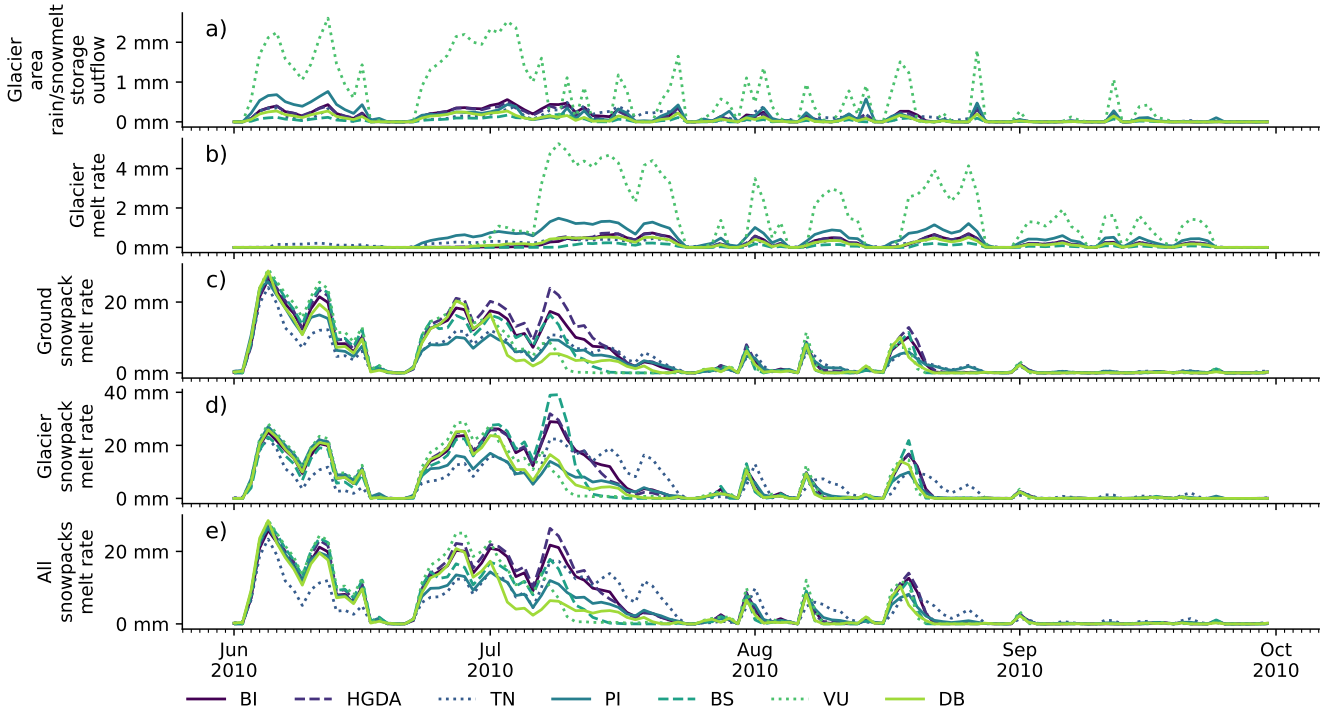

Figure S16. Modeled water fluxes rates due to a) outflow of the glacier area rain/snowmelt storage, b) glacier melt rate, c) ground snowpack melt rate, d) glacier snowpack melt rate and e) global snow melt rate during the summer 2010. Melt rates are computed on their respective areas.

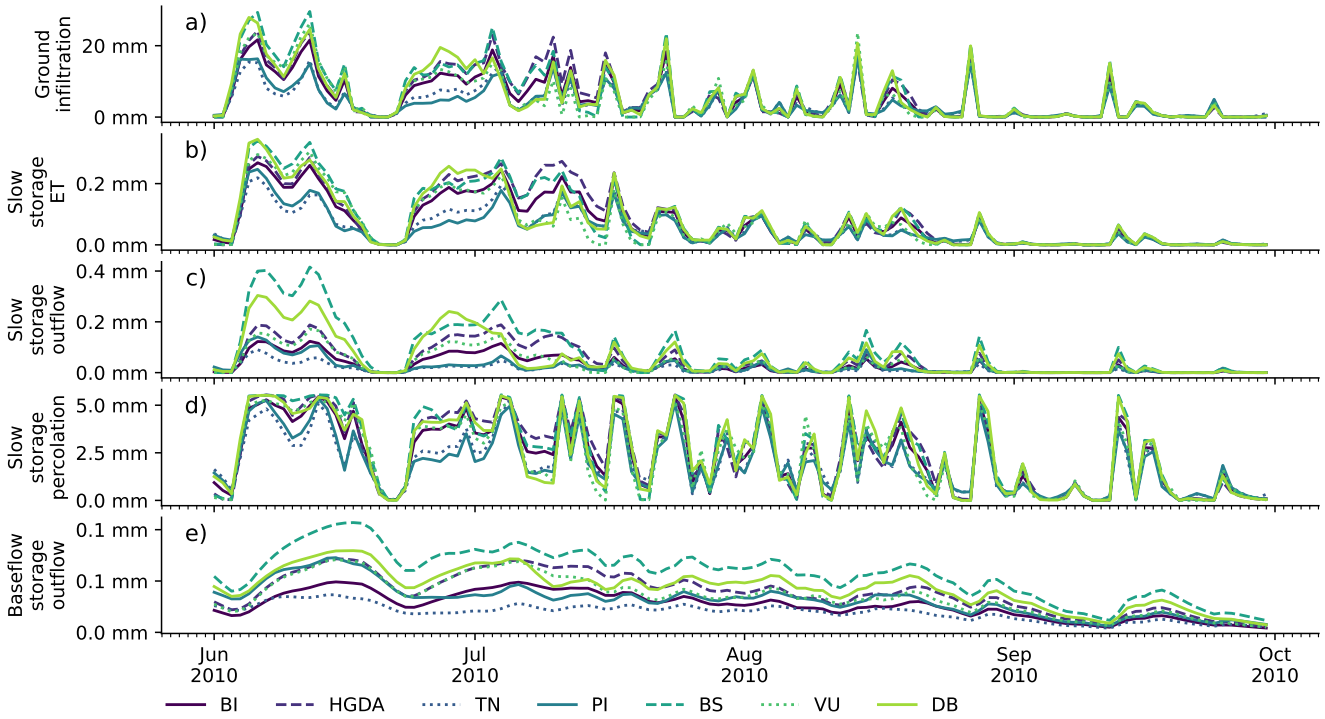

Figure S17. Modeled water fluxes rates due to a) ground infiltration into the slow storage, b) evapotranspiration and c) runoff out of the slow storage, d) percolation from the slow storage, into the baseflow storage and e) runoff out of the baseflow storage during the summer 2010. All these rates are computed on the ground areas only.

S9. NSE and KGE metrics

S9.1. Aid to understand NSE and KGE behavior

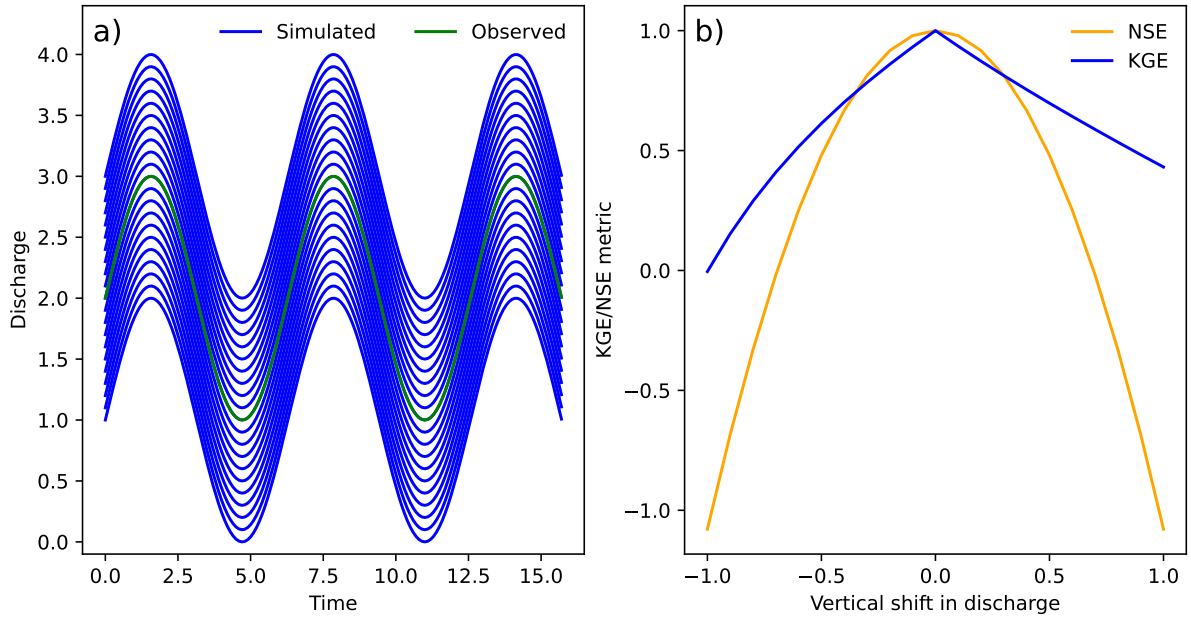

Figure S18. a) Vertical shift between the observed and simulated discharges, and b) the associated changes in NSE and KGE.

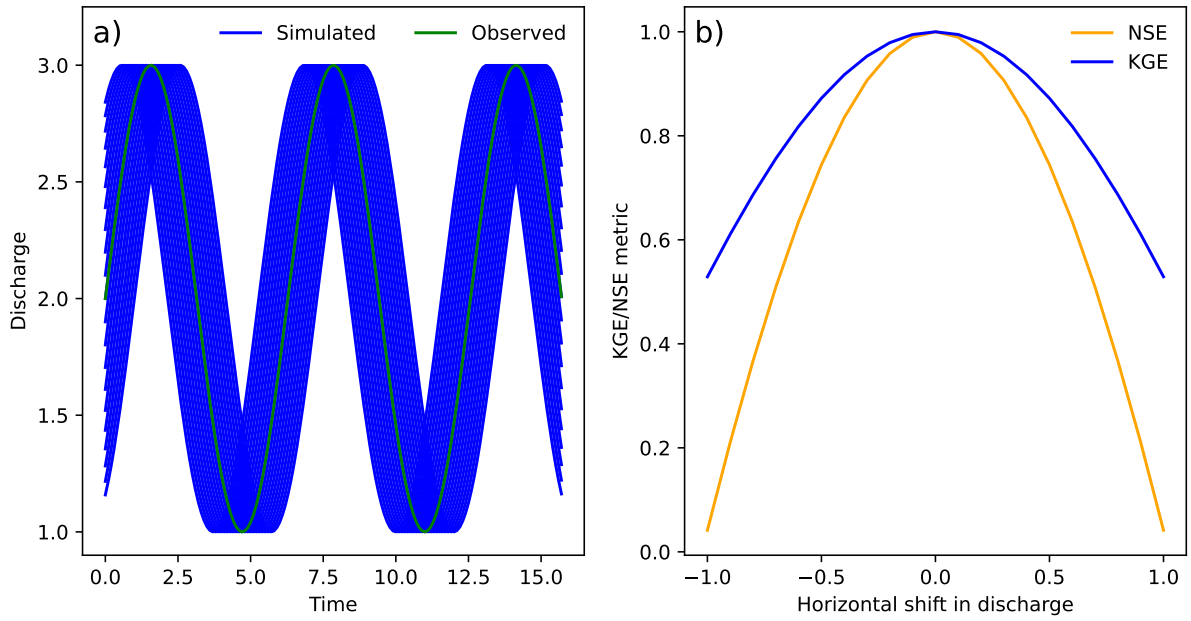

Figure S19. a) Horizontal shift between the observed and simulated discharges, and b) the associated changes in NSE and KGE.

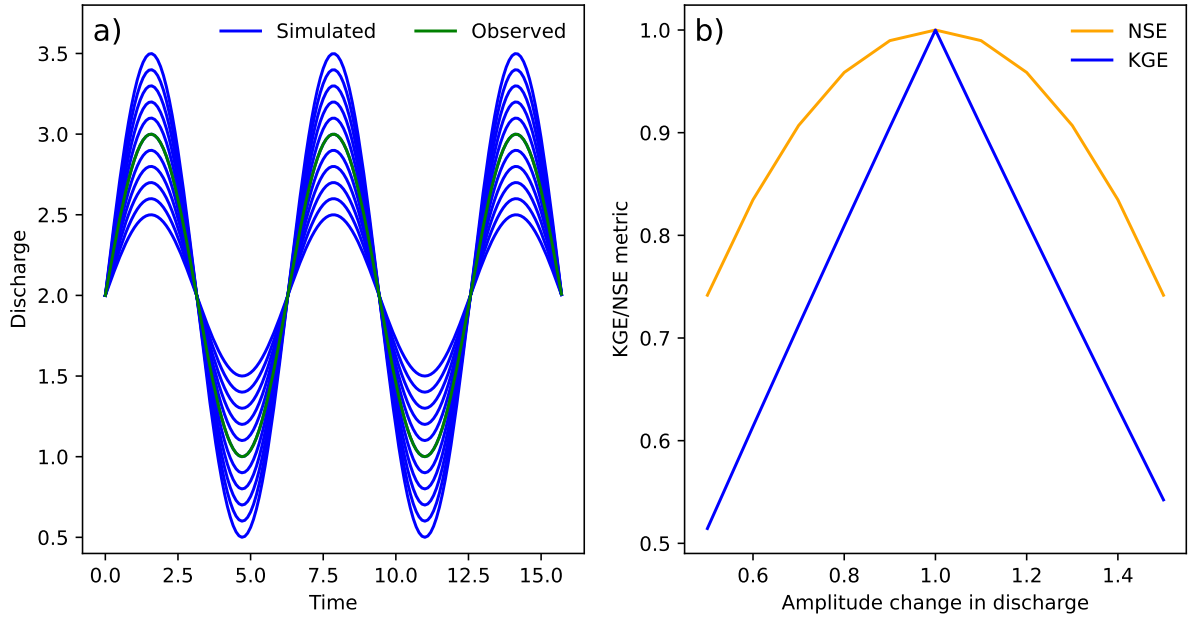

Figure S20. a) Amplitude change between the observed and simulated discharges, and b) the associated changes in NSE and KGE.

S9.2. KGE vs NSE scoring

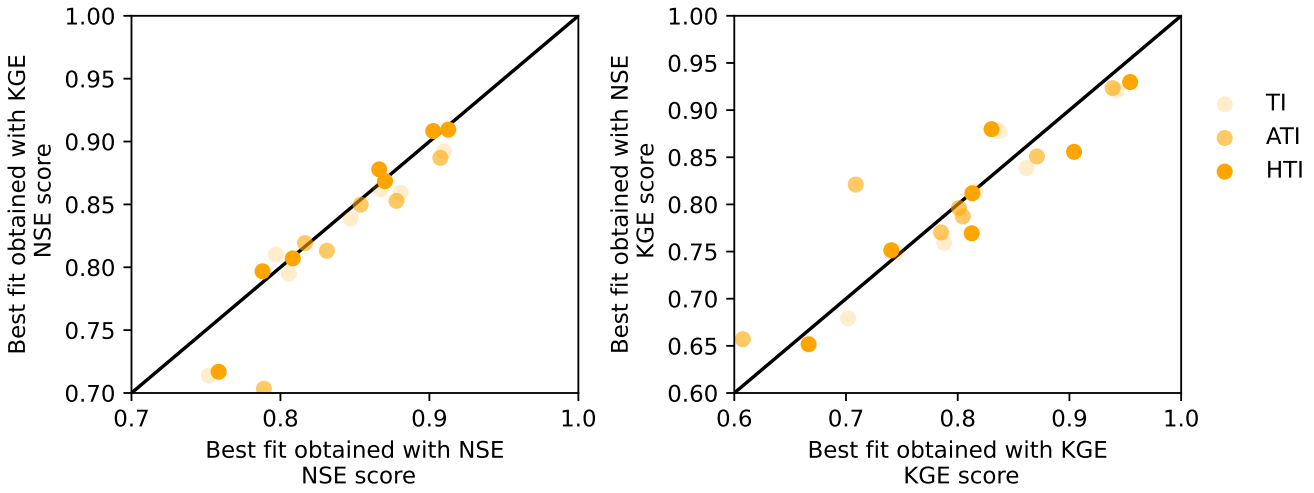

Figure S21. Comparison of the performance of the two NSE and KGE performance criteria in finding the calibrated parameters that are then transferred onto the different catchments. In x the NSE/KGE score when transferred with parameters obtained through NSE/KGE, rep. calibration, and in y the opposite.

S9.3. Resampling and bootstrapping

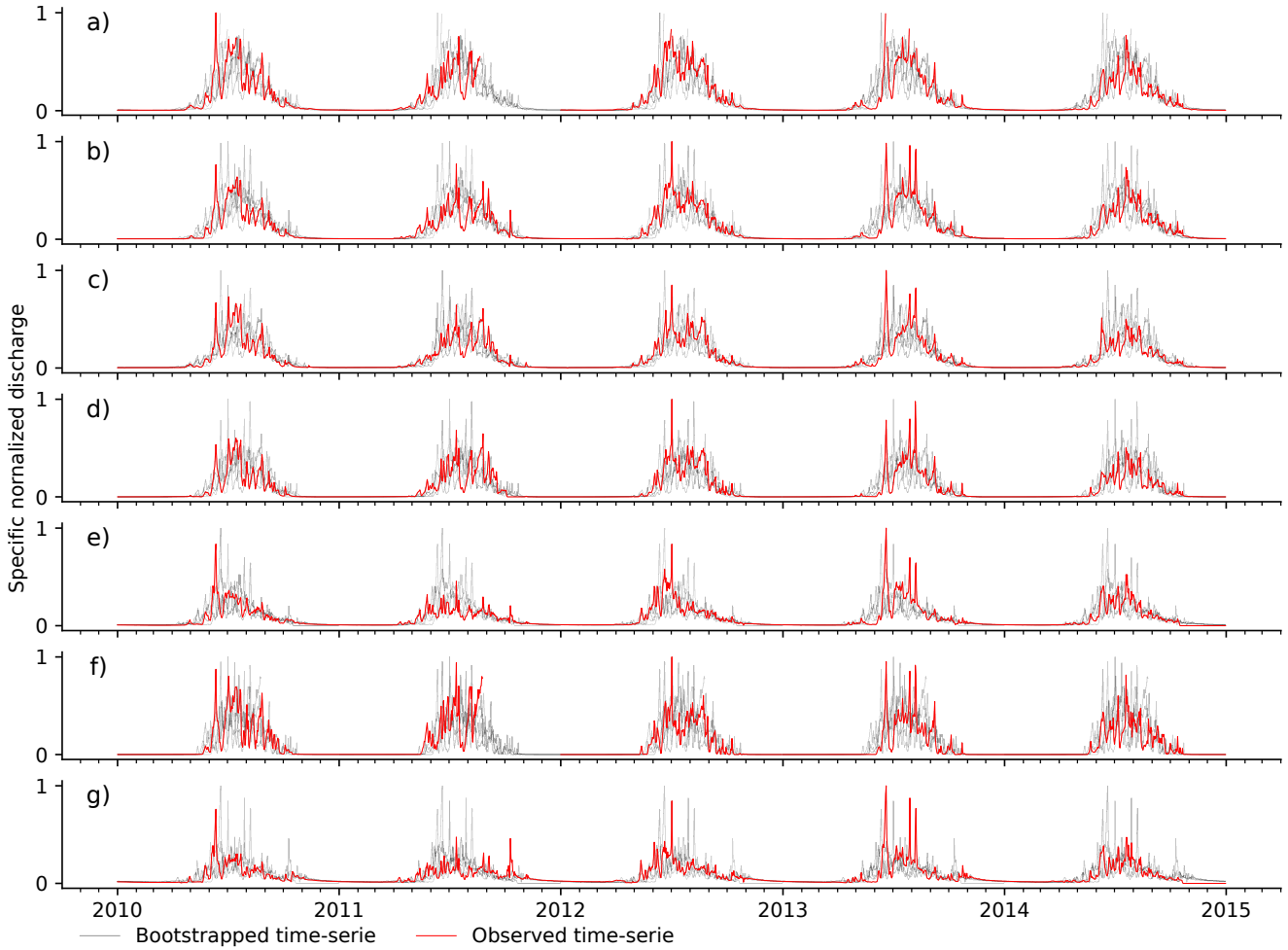

Figure S22. Comparison of resampled discharge time-series with observed discharge time-series for all catchments. Resampled time-series are obtained by exhaustively replacing each year's discharge with the discharge observed during one year of the 2010-2014 period in the same catchment.

S9.4. Comparison of different benchmark metrics

	NSE		KGE	
Catchment	5-year resample	46-year bootstrap	5-year resample	46-year bootstrap
BI	0.619	0.516	0.801	0.759
HGDA	0.597	0.578	0.794	0.731
TN	0.576	0.531	0.783	0.701
PI	0.502	0.474	0.746	0.689
BS	0.406	0.405	0.697	0.670
VU	0.429	0.372	0.710	0.662
DB	0.220	0.193	0.603	0.422

Table S4. Results of the different benchmarking methods for the NSE and the KGE. The 5-year exhaustive resampling is done by using all possible combinations of the simulated years 2010-2014 (5 years: 3125 combinations). The 46-year bootstrapping is done by randomly selecting 3125 combinations from the 1969-2014 discharge data.

References

Fischer, M., Huss, M., Barboux, C., and Hoelzle, M.: The new Swiss Glacier Inventory SGI2010: Relevance of using high-resolution source data in areas dominated by very small glaciers, Arctic, Antarctic, and Alpine Research, 46, 933–945, https://doi.org/10.1657/1938-4246-46.4.933, 2014.

Linsbauer, A., Huss, M., Hodel, E., Bauder, A., Fischer, M., Weidmann, Y., Bärtschi, H., and Schmassmann, E.: The New Swiss Glacier Inventory SGI2016: From a Topographical to a Glaciological Dataset, Frontiers in Earth Science, 9, https://doi.org/10.3389/feart.2021.704189, 2021.

Shokory, J. A. N. and Lane, S. N.: Patterns and drivers of glacier debris-cover development in the Afghanistan Hindu Kush Himalaya, Journal of Glaciology, 69, 1260–1274, https://doi.org/10.1017/jog.2023.14, 2023.

Shokory, J. A. N., Horton, P., Schaefli, B., and Lane, S. N.: Glacier-influenced hydrological regimes of Afghanistan Hindu Kush Himalaya (AHKH) under current and future climate, Ph.D. thesis, UNIL, 2023.

Swift, D. A., Nienow, P. W., Hoey, T. B., and Mair, D. W.: Seasonal evolution of runoff from Haut Glacier d'Arolla, Switzerland and implications for glacial geomorphic processes, Journal of Hydrology, 309, 133–148, https://doi.org/10.1016/j.jhydrol.2004.11.016, 2005.

SwissTopo: SwissTopo - Geological vector datasets (GeoCover), SwissTopo - Swiss Federal Office of Topography, https://www.swisstopo.admin.ch/en/geological-model-2d-geocover, version 2., 2024.